Soft Matter

PAPER

View Article Online
View Journal | View Issue

Cite this: *Soft Matter*, 2016, 12, 8755

Anisotropic magnetic particles in a magnetic field

Ilya Martchenko,[ab] Jérôme J. Crassous,*[a] Adriana M. Mihut,[a] Erik Bialik,†[a] Ann M. Hirt,[c] Chantal Rufier,[b] Andreas Menzel,[d] Hervé Dietsch,‡[b] Per Linse[a] and Peter Schurtenberger*[a]

Received 20th June 2016,
Accepted 21st September 2016

DOI: 10.1039/c6sm01411a

www.rsc.org/softmatter

We characterize the structural properties of magnetic ellipsoidal hematite colloids with an aspect ratio $\rho \approx 2.3$ using a combination of small-angle X-ray scattering and computer simulations. The evolution of the phase diagram with packing fraction ϕ and the strength of an applied magnetic field B is described, and the coupling between orientational order of magnetic ellipsoids and the bulk magnetic behavior of their suspension addressed. We establish quantitative structural criteria for the different phase and arrest transitions and map distinct isotropic, polarized non-nematic, and nematic phases over an extended range in the ϕ–B coordinates. We show that upon a rotational arrest of the ellipsoids around $\phi = 0.59$, the bulk magnetic behavior of their suspension switches from superparamagnetic to ordered weakly ferromagnetic. If densely packed and arrested, these magnetic particles thus provide persisting remanent magnetization of the suspension. By exploring structural and magnetic properties together, we extend the often used colloid-atom analogy to the case of magnetic spins.

1 Introduction

While the phase behavior of spherical particles is well understood, present research interests focus on anisotropic colloids.[1] For ellipsoids and rods, for example, with growing packing fraction ϕ of particles, the contribution of the mixing entropy associated to particle excluded volume will exceed the contribution of orientational entropy at some point, and trigger an isotropic–nematic (I–N) transition. The classical theory of Onsager predicts the conditions for the I–N transition in infinitely long rods[2,3] and early simulations by Frenkel *et al.* described the isotropic–nematic transitions in suspensions of hard ellipsoids of varied aspect ratios.[4–6] At even higher packing fractions, the ellipsoids undergo a fluid–solid transition and crystallize or get jammed. Numerous numerical simulations of hard ellipsoids have been developed over the last decade.[7–12]

Of special interest are prolate ellipsoids with low aspect ratios ρ in the range $2 < \rho < 2.75$. Here the I–N transition is shifted to much higher packing fractions, and an additional solid phase recently identified by Pfleiderer *et al.*[11,12] as an oriented simple monoclinic crystal occurs at very high packing fractions. It is important to note that the packing fraction ϕ_N, where the I–N transition occurs and the packing fraction ϕ_C, where crystallization occurs approach each other as the aspect ratio decreases.[8] For an aspect ratio between 2 and 2.75, these two points coalesce and simulations predict a direct isotropic–crystalline transition with a broad coexistence region. There is, however, still only a limited, albeit growing number of experimental reports on well defined model systems of ellipsoids available in the literature.[13–20] This is partly due to the difficulty of finding suitable model systems. Ideally, model particles should be monodisperse, have tuneable axial ratios to reach the desired areas in the phase diagram, and a well-defined and possibly adjustable interaction potential.

Another interest in anisotropic particles arises from the fact that they offer control over one or several rotational degrees of freedom through the application of external magnetic and/or electric fields. Recent experimental work by Shah *et al.* shows an example of such a field-assisted phase transition, where the nematic order of ellipsoids was promoted by an electric field.[13] However, care has to be taken when choosing the experimental system, as an external field can not only constrain rotational motion, but may also lead to strong dipolar interactions that then also result in enhanced field-driven self assembly.[15,21–24] Therefore, attempts to use external fields in order to restrict rotational degrees of freedom only will require particles that are able to respond to an externally applied field, but have a magnetic susceptibility or optical polarisability that is small enough to not result in significant dipolar interactions.

[a] Division of Physical Chemistry, Department of Chemistry, Lund University, Lund, Sweden. E-mail: jerome.crassous@fkem1.lu.se, peter.schurtenberger@fkem1.lu.se
[b] Adolphe Merkle Institute and Fribourg Center for Nanomaterials, University of Fribourg, Fribourg, Switzerland
[c] Institut fur Geophysik, ETH Zurich, Zurich, Switzerland
[d] Swiss Light Source, Paul Scherrer Institute, Villigen, Switzerland
† Present address: Molecules in Motion, Åkerbyvägen 390, 18738 Täby, Sweden.
‡ Present address: BASF SE, Modelling and Formulation Research, Formulation Platform, 67056 Ludwisghafen am Rhein, Germany.

We have thus performed a systematic investigation of the phase behaviour and structural properties of dense suspensions of ellipsoidal particles using silica-coated hematite particles as a suitable model system. Hematite colloids can easily be fabricated into various shapes such as almost monodisperse ellipsoids.[25] An appropriate coating with silica and functionalisation through an additional polyelectrolyte layer then renders them highly stable even at very high densities, and over a large range of solvent conditions such as pH and ionic strength.[20]

In this study, we use silica-coated hematite ellipsoids, with a hematite core with an average length $L_C = 227 \pm 42$ nm, short axis $d_C = 51 \pm 9$ nm, and shell thickness of 28 ± 3 nm, additionally stabilised by a PAA layer with a thickness of approximately 17 nm. The particles thus have an overall length $L \approx 320$ nm and an axial ratio $\rho \approx 2.3$. The weakly ferromagnetic core of the ellipsoids provides a permanent dipole of the individual particle that lays in the short (equatorial) axis of the ellipsoid and thus allows for a external control of the rotational degrees of freedom of each particle.[17,18] When investigating these particles in an external magnetic field, it is essential to understand the effect of the field on both the orientational distribution and the interparticle interactions. In our case we can easily estimate the latter from a simple calculation based on the known magnetic properties of these colloids.[17] Although the magnetic moment is sufficient for the particle to surpass Brownian relaxation in moderate magnetic fields,[17] the dipole–dipole interparticle interaction is weak. Indeed, for two dipoles with equal moments $\mu = 1.3 \times 10^{-18}$ A m^2 and separated by a distance r, the potential energy

$$E_d = \frac{\mu_0}{4\pi} \times \frac{\mu^2}{r^3}, \quad (1)$$

exceeds thermal energy k_BT at room temperature only if $r < 30$ nm. Such a separation is significantly shorter than the minimum non-magnetic spacing between the hematite cores created by the combined silica and PAA shells. We can thus conclude that magnetic dipolar interaction will be negligible, and the field will then only influence the rotational degrees of freedom.

We have used these particles as model systems for the following reasons. Firstly, they can be made at relatively low axial ratios, *i.e.* a degree of anisotropy where simulations have indicated a rather complex phase diagram with a possible coexistence of a fluid, a nematic and a crystalline (simple monoclinic, SM2) phase.[9,26] Secondly, an external magnetic field can be applied in order to control rotational motion and investigate the influence of a reduction in the rotational degree of freedom of the particles on the phase behaviour.[17,18] Finally, these particles allow us to investigate the link between the bulk magnetic properties of dense suspensions and the local structural and orientational order.

In the following sections we present results from an experimental investigation of the alignment and constrained motion of these particles as a function of packing fractions ϕ and external magnetic field strength B. We employ X-ray scattering experiments to investigate the positional and orientational order developing at high packing fractions with and without a directing field. The experimental results are compared with the findings from systematic Monte Carlo computer simulations. Additionally, we use magnetometry to characterize the magnetic properties of the resulting suspensions. In a last step, we discuss the analogies between the behavior of geometrically arrested colloidal magnetic dipoles and classical examples of magnetic transitions in condensed matter systems of atomic spins.

2 Materials and methods

Chemicals

Iron(III) perchlorate hexahydrate ($Fe(ClO_4)_3{\cdot}6H_2O$), polyvinylpyrrolidone (PVP, 10 000 g mol^{-1}), tetramethylammonium hydroxide (TMAH), and polyacrylic acid (PAA, 100 000 g mol^{-1}) were purchased from Sigma Aldrich and used as received. Sodium dihydrogen phosphate monohydrate ($NaH_2PO_4{\cdot}H_2O$) and urea from Fluka, tetraethyl orthosilicate (TEOS) from Merck, 3-aminopropyl tetraethoxysilane (APTES) from ABCR, and absolute ethanol from Fluka were also used without further purification. Ultra-pure water (18.2 MΩ cm resistivity) purified with a MilliQ system was used throughout all experiments.

Synthesis

The particles were synthesized *via* the route developed by Rufier *et al.* as described in detail previously in ref. 20. In the first step, spindle-type hematite nanoparticles[27] were fabricated and used as a template for further coating with silica and PAA. In a typical synthesis, a 2 L glass bottle was filled with 92.4 g of $Fe(ClO_4)_3{\cdot}6H_2O$ (200 mmol), 1.3 g of $NaH_2PO_4{\cdot}H_2O$ (9.4 mmol, *i.e.*, with molar ratio $NaH_2PO_4/Fe^{3+} = 0.047$), and 12 g of urea $(NH_2)_2CO$ (0.2 mol) in 2 L of ultra pure water, and then sonicated until a homogeneous solution was achieved. The solution was kept in a preheated oven at 98 °C for 24 h. Approximately 2 g of a brown sediment of particles was obtained in a brownish suspension. The supernatant was decanted, and the precipitate was cleaned by seven successive cycles of washing with pure water and centrifugation at 13 000 rpm for 10 min. Finally, approximately 2 g of hematite nanoparticles were recovered and dispersed into 40 mL of water.

In the second step, PAA-silica coating was performed using APTES and PAA. To stabilize the particles during the coating, PVP was adsorbed onto the surface of hematite particles,[28] using the following procedure: in a 1 L container, 100 mg of spindle hematite particles and 2 g of PVP were dispersed in 220 mL of pure water. The particles were sonicated for 2 h and then mechanically stirred for 15 h. The nanoparticles were centrifuged for 10 min at 13 000 rpm and redispersed in 10 mL water. The PVP stabilized hematite particles were dispersed in 10 mL of water. The particle suspension (*i.e.*, containing 100 mg of hematite particles) was then added to ethanol (225 g) in a 500 mL plastic bottle followed by sonication and mechanical stirring at 400 rpm. 85 mg of TMAH in 3 mL of ethanol was added to the nanoparticle suspension. After 30 min of stirring, 250 μL of TEOS in 1 mL of ethanol was added at once. A mixture

of 20 μL of APTES and 750 μL of TEOS in 3 mL of ethanol was then injected in 3 portions every 30 min. The suspension was allowed to stand for 30 min, and then PAA (100 kg mol^{-1}) (270 μL in 1 mL of ethanol) was added. Sonication was applied for two hours after the last injection, and the dispersion was stirred overnight at room temperature.

In order to acquire the necessary amount of material, the synthesis of PAA-silica-hematite particles was repeated four times. The resulting, nearly identical, batches were used for two separate synchrotron beamtimes, and labeled A1, B1, B2, B3 (with A and B denoting the beamtimes, respectively).

Transmission electron microscopy (TEM)

A TEM-CM100 microscope from Philips operating at 80 keV was used to visualize the coronal sections of the ellipsoidal particles deposited on a carbon coated, 300 mesh, grid. Lengths L and diameters d were measured for a set of 440 particles and then analyzed statistically.

Thermogravimetric analysis (TGA)

The mass fractions of the suspensions were determined with a TGA/DSC STAR^e System from Mettler-Toledo GmbH. The samples were filled into 40 μL aluminum crucibles, heated in air at a rate of 10 °C min^{-1} to 120 °C and then kept at 120 °C for 2 h. The masses of initial dispersions and dried particles were measured with a precision of *ca.* 10^{-3} mg.

Small-angle X-ray scattering (SAXS)

Aqueous dispersions of magnetic ellipsoids were investigated in the presence of external magnetic fields. To reach a broader q-range, the scattering experiments were carried out at the cSAXS beamline of the Swiss Light Source (Paul Scherrer Institute, Switzerland) with a sample-detector distance of 7 m and an energy of 11.2 keV (corresponding to a wavelength of λ = 0.111 nm). The scattering patterns were recorded with acquisition times between 0.1 and 0.2 s on a single-photon counting PILATUS detector (1475 × 1679 pixels). The samples were sealed in quartz capillaries of 1 mm diameter and 0.1 mm wall thickness, and investigated at room temperature. The horizontal magnetic field was produced with a water-thermostated electromagnet such that the field lines were always normal to the incident beam. The SAXS experiments were performed during two separate beamtimes.

In beamtime A, we studied the particles in a complete 5-branch hysteresis loop with steps of 0.04 T (initially with the field ascending from 0 T to 1 T; then with the field descending from 1 T to 0 T and further to −1 T, *i.e.* reversing the direction of the field; and finally returning to zero field and ascending up to 1 T).

In beamtime B, we focused on the low-field behavior for a broader range of packing fractions and studied the particles in 2-branch hysteresis loops with steps of 0.008 T (increasing the field from 0 T to 0.23 T, and then returning to 0 T).

The resulting anisotropic scattering data was then analysed on 12 (beamtime A) and 36 (beamtime B) discrete sectors of the acquired 2D scattering patterns in the corresponding range of $0.01 < q < 1\ nm^{-1}$, where q is the magnitude of the scattering vector. The resulting scattering curves were treated following standard procedure (background subtraction and normalization).

Magnetometry

Magnetic hysteresis loops were measured for the batches B1, B2, and B3 with a vibrating sample magnetometer MicroMag 3900 from Princeton Measurements Corporation. Liquid samples were sealed in 3 mm cylindrical quartz cells and measured at 295 K. In a standard procedure, each sample was brought to a field of 1 T; then the direct magnetic moment of the bulk sample was measured at intermediate fields down to −1 T, followed by bringing the sample back to 0 T and then a field of 1 T. Averaging time was 0.1 s. Remanent magnetization was measured on a three-axis, 2G SQUID rock magnetometer.

Monte Carlo simulations

Metropolis Monte Carlo (MC) simulations were performed for a fluid of hard monodisperse prolate ellipsoids with axial ratio p = 2.3. The number of particles was 2268 in all simulations, corresponding to an fcc lattice with 7 × 9 × 9 unit cells and four particles each, and the density was adjusted by varying the box size accordingly. Particle overlap was tested using the Perram–Wertheim algorithm.[29] No interparticle dipolar interactions were considered. This corresponds to weakly magnetic particles in a strong magnetic field, which is the situation in the experiments.

3 Results and discussion

3.1 Single particle properties

In a first step, we characterize the morphology and dimensions of the particles. The TEM micrograph in Fig. 1 shows a representative example of the ellipsoidal particles employed for the study. Their characteristic dimensions were determined from a random selection of 440 particles, and found to be moderately polydisperse and well described by Gaussian distributions.[19] The resulting values for the different structural elements are: the hematite core (full long axis L_C = 227 ± 42 nm, full short axis d_C = 51 ± 9 nm), the silica shell (polar thickness 30 ± 4 nm, equatorial thickness 27 ± 3 nm), while the PAA layer is invisible

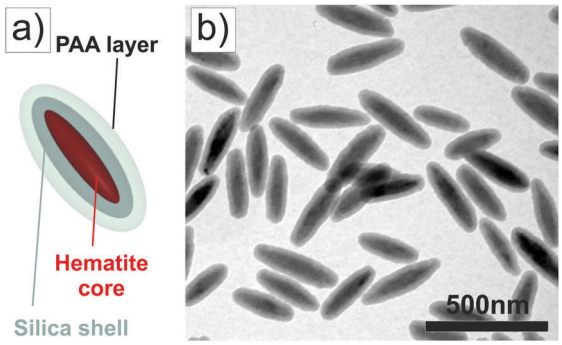

Fig. 1 (a) Schematic description and (b) TEM micrograph of the model ellipsoids (see Materials and methods for details).

for the beam of electrons. The overall size distributions of the solid core–shell particles were: length or long axis $L_P = 287 \pm 41$ nm and diameter or short axis $d_P = 105 \pm 8$ nm, with an aspect ratio of 2.7 ± 0.3. Here the dimensions are presented as $x \pm \delta x$ where x is the population mean and δx is standard deviation of the statistical data set.

We combine the statistical data set of the dimensions of each particle with our previous results[17] on the density and porosity of the building blocks. Here we consider a volume fraction 0.26 of silica-filled pores inside hematite, hematite density 5.26 g cm^{-3}, and silica density 1.90 g cm^{-3}. The average mass density of a single solid particle is then $\rho_p = 2.381 \pm 0.007$ g cm^{-3}, while the average mass fraction of hematite $\alpha = m_{hem}/m_p$ inside a particle is $\alpha = 0.307 \pm 0.003$.

While the solid Fe_2O_3 core and SiO_2 shell have known dimensions and density, special attention is needed to characterize the effective dimensions of the PAA layer which increases the excluded volume and decreases the hydrodynamic aspect ratio of each particle. We first determine the nominal packing fraction for solid (hematite-silica) ellipsoids, without considering the PAA layer, based on the known mass fractions of suspensions and particle density. We then use space-filling considerations and determine a correction factor ξ that gives the effective hydrodynamic packing fraction:

$$\phi = \xi \times \frac{c \cdot \rho_w}{(1-c)\cdot \rho_p + c \cdot \rho_w}, \quad (2)$$

where ρ_w is the mass density of water ($\rho_w = 1$ g cm^{-3}), and c is the mass fraction of the dispersion ($0 < c < 1$). The highest achievable packing fraction of ellipsoids with $p > 1.7$ is 0.7707, as predicted theoretically.[30] We make an assumption that our densest sample (solid packing fraction 0.3865), obtained *via* repeated centrifugation cycles, reaches the said packing fraction of $\phi = 0.7707$. This leads to $\xi = 1.994$, a hydrodynamic PAA layer thickness of 17.3 nm, a hydrodynamic aspect ratio of $p = 2.3 \pm 0.2$, a hydrodynamic length of $L_H = 321 \pm 21$ nm, a hydrodynamic diameter $d_H = 140 \pm 8$ nm, and a resulting hydrodynamic dimension $2R_H = 196 \pm 17$ nm. It is possible to independently determine the apparent hydrodynamic thickness of the PAA layer *via* dynamic light scattering in dilute conditions. The resulting value, 26 nm, is found to exceed the value obtained from packing considerations. However, it is important to realize that the difference between the two estimates of the particle hydrodynamic size is approximately 5% in terms of particle length, which falls well within an inherent experimental error and is significantly smaller than the length polydispersity of the particles. In ref. 19 we analyzed such a situation in detail by comparing TEM-based dimensions with translational and rotational diffusion coefficients determined by polarized and depolarized dynamic light scattering. We therefore believe that the space-filling considerations provide the most accurate estimate of packing fractions ϕ with a possible trend to overestimate ϕ. Note that $\phi = \frac{\pi}{6} n_P$, where n_P is the dimensionless number density used in ref. 5 and other theoretical works.

3.2 Magnetic field-driven assembly of hematite particles

In a next step, we can now investigate the influence of an external magnetic field on the resulting structural properties of particle suspensions at different values of ϕ and B using small-angle X-ray scattering (SAXS) measurements.

The basic scattering geometry and a definition of the coordinate frame are shown in Fig. 2. Typical examples from the results of SAXS measurements with dense particle suspensions without and with an applied magnetic field are shown in Fig. 3. Fig. 3a, c, e, g and i show the scattering patterns from particle dispersions at zero-field and with increasing volume fraction ϕ, while those with an applied field of $B = 0.23$ T are shown in Fig. 3b, d, f, h and j. At the lowest $\phi = 0.008$, interparticle interactions are negligible, and the scattering pattern for $B = 0$ is completely isotropic and reflects the particle form factor only. Upon the application of a sufficiently high magnetic field, the particles align, and the scattering pattern becomes highly anisotropic along the field (x-) axis, as the particles now are aligned with their magnetic moment (parallel to the short particle axis, *i.e.*, normal to the c crystallographic axis) along the field, while the long axis of each particle is able to freely rotate around the μ (or B) axis in the yz-plane (Fig. 2a).[17] At zero field, with increasing ϕ the particle suspensions develop strong structural correlations that initially result in a clearly visible isotropic liquid-like structure factor peak on a characteristic length scale of approximately the particle short axis (Fig. 3c and e). Upon the application of the magnetic field, the scattering pattern again becomes highly anisotropic, but now with an intense structural peak along the field direction, and an additional weaker split peak perpendicular to the field direction, where the second peak at lower q-values is of order length scale of the particle length (Fig. 3f). Without attempting initially any quantitative analysis of the scattering patterns, this indicates a field-induced nematic-type ordering in the sample. When returning to zero-field the system returns to the initial

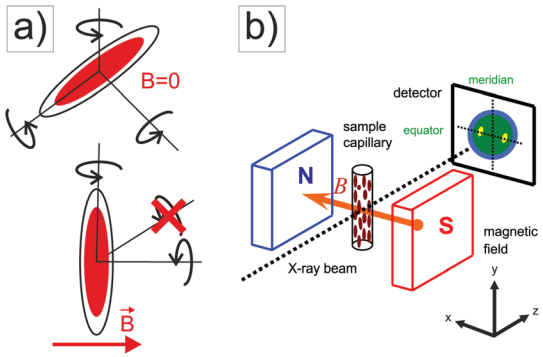

Fig. 2 (a) Effect of an applied magnetic field of strength B on the orientation of the magnetic ellipsoids. The particles are aligned with their magnetic moment (parallel to the short particle axis) along the field, while the long axis of each particle is able to freely rotate around the B axis. (b) Geometry of the SAXS experiment and definition of the lab frame system. The direction of the uniform magnetic field is in the x-axis, which is always normal to the incident X-ray beam along the z-axis. The scattered X-rays are then recorded on the detector in the x–y-plane.

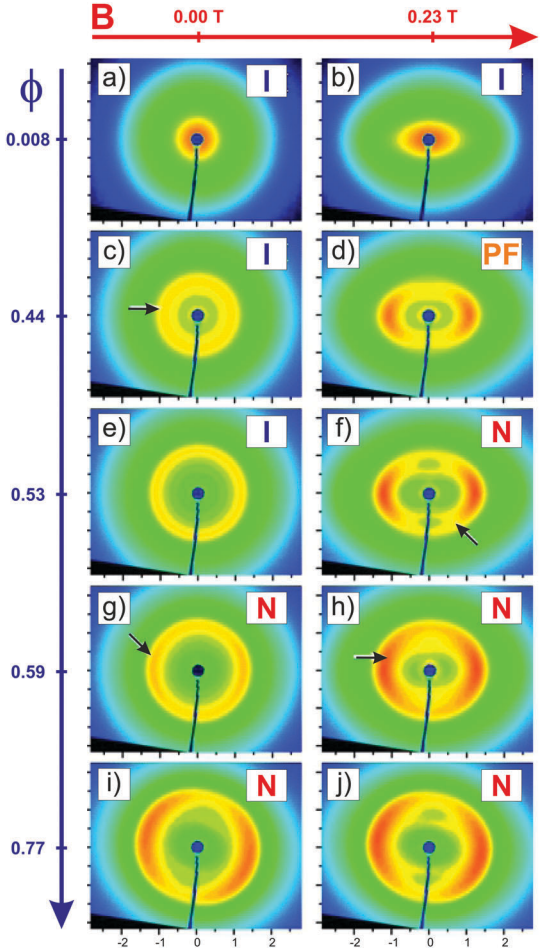

Fig. 3 Two-dimensional SAXS scattering patterns of ellipsoids at a range of packing fractions, without (a, c, e, g and i) and with an applied uniform external magnetic field of B = 0.23 T (b, d, f, h and j). Volume fractions are ϕ = 0.008 (a and b), ϕ = 0.044 (c and d), ϕ = 0.053 (e and f), ϕ = 0.59 (g and h), and ϕ = 0.77 (i and j), Specific features of the patterns in the equatorial and meridian planes are marked with arrows and discussed in the text. The scale on all patterns is in units of $qd/2\pi$, where d = 139.9 nm is the particle short axis including the PAA shell. Also shown is the location (I,PF,N) of the corresponding sample in the phase diagram.

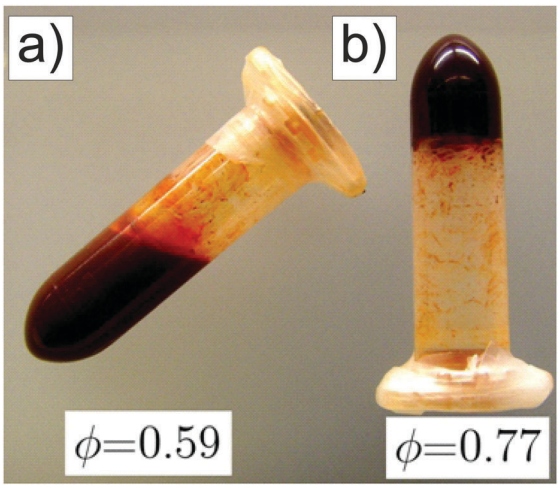

Fig. 4 (a) Fluid-like behavior of the ellipsoids at ϕ = 0.59. (b) Arrested or solid-like behavior of the ellipsoids at ϕ = 0.77.

state dominated by thermal relaxation and no preferential direction remains (data not shown).

However, at ϕ = 0.59 the situation changes, and we now observe a weakly anisotropic scattering pattern already at zero field (Fig. 3g). This indicates a preferential orientation and the formation of at least partial nematic order in the system. It is worth noting that the initial axis of symmetry at zero-field often appears in the x-axis or the horizontal direction in the sample. We relate this fact to the unidirectional viscous shear flow that contributes to partial pre-alignment of the long axes of the particles along the capillary wall, *i.e.* in the y-axis. In the dilute samples, such pre-alignment is instantaneously cancelled by Brownian relaxation and plays no role. In the dense and highly viscous samples, however, the shear may orient individual nematic domains and may thus be the reason for the persisting preferred vertical orientation of the particles and the observed positional correlation in the horizontal direction. The application of a magnetic field to this sample then strongly enhances the positional and orientational order. Moreover, after returning to zero field, the system does not completely relax, and increased order remains. At the highest packing fraction of ϕ = 0.77, the scattering pattern on the detector exhibits distinct zero-field structure peaks in the y-axis, indicating positional correlations in the particle array in this direction (Fig. 3i). These features are promoted with increasing field (Fig. 3j) and persist as the field is removed. A closer inspection of the macroscopic flow behaviour of the two samples with highest concentrations also shows (Fig. 4) that the suspension at ϕ = 0.59 is a highly viscous fluid, while the suspension at ϕ = 0.77 is solid-like or arrested.

Analysing, interpreting and comparing the 2D scattering patterns of different samples is not straightforward for anisotropic systems. For isotropic particles this can easily be done using static structure factors $S(q)$ as a measure of the degree of positional correlations induced by interparticle interactions. For anisotropic particles we now need to take into account the coupling between the orientation-dependent particle form factor and the positional and orientational correlations between different particles. In the case of samples, where the scattering pattern is still isotropic such as the one shown in Fig. 3c, we can define an effective or measured structure factor $S_M(q)$. Here $S_M(q)$ is obtained by dividing the concentration-normalised scattering intensity of the correlated sample with the concentration-normalised intensity from a highly dilute non-interacting sample analogous to the way a structure factor for spherical particles is determined. For anisotropic samples with strong positional correlations, such as the ones shown in Fig. 3f–j, this no longer, however, makes sense. We have to devise another strategy, which we illustrate in Fig. 5, using the scattering pattern obtained with the sample with the highest concentration ϕ = 0.77 and an applied field with B = 0.23 T.

The 2D pattern shows clear structural correlations along the field axis (equatorial or x-axis), as well as two peaks along the

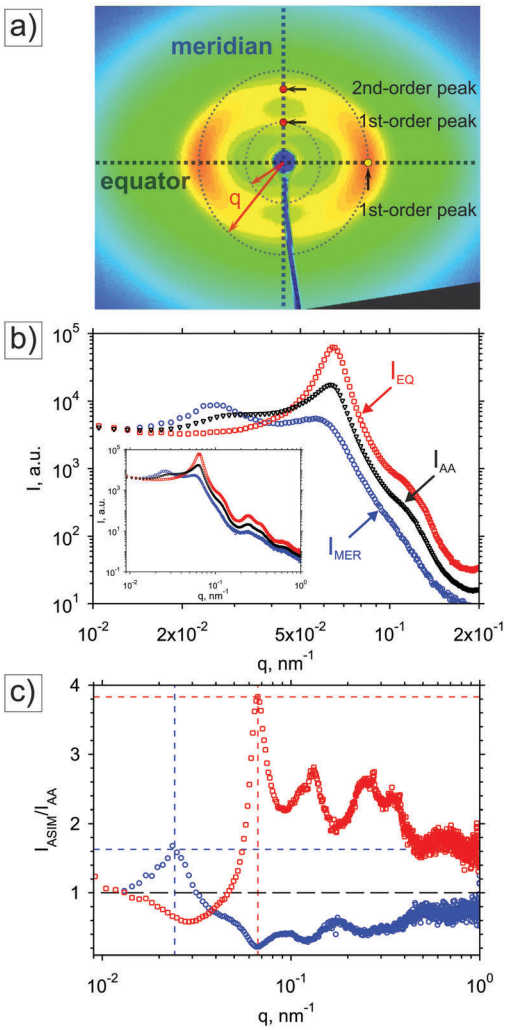

Fig. 5 Anisotropic scattering pattern for a strongly correlated sample with ϕ = 0.77 and an applied field with B = 0.23 T. (a) 2D scattering pattern with the characteristic axes of symmetry in the plane of the detector: equator (x-axis) and meridian (y-axis). The typical correlation peaks and the corresponding scattering vectors q are highlighted by arrows. (b) The anisotropic scattering curves $I_{EQ}(q)$ in the equatorial direction (open squares) and $I_{MER}(q)$ in meridian direction (open circles) normalised by the azimuthally averaged curve $I_{AA}(q)$ (open triangles). Shown is data only for a range of scattering vectors $q \leq 0.2$ nm^{-1}, where the data in effect reflects structural correlations, whereas the higher-q data is completely dominated by the internal core–shell structure. The full scattering curves are shown in the inset. (c) The normalised anisotropic scattering intensities I_{ASIM}/I_{AA} given by the ratios $I_{EQ}/I_{AA}(q)$ and $I_{MER}/I_{AA}(q)$ emphasize the anisotropic features seen in the 2D scattering pattern.

meridian or y-axis. A quick calculation shows that they appear at characteristic length scales of $2\pi/q_{EQ}^* \approx 100$ nm and $2\pi/q_{MER}^* \approx 280$ nm, where $2\pi/q_{EQ}^*$ is the position of the first order peak along the equatorial axis and $2\pi/q_{MER}^*$ is the position of the first order peak along the meridian axis. They are thus related to the translational order of the short axis and the long axis of the ellipsoids, respectively. In order to quantify the degree of anisotropy and structural correlations and obtain simple effective order parameters that we can compare for different samples, but also with predictions based on computer simulations, we first determine the q-dependence of the scattered intensity along two principal axes as defined in Fig. 5a. Here we follow an approach previously used to analyze field-induced and mechanical alignment of block copolymers.[31]

The resulting 1D scattering curves are shown in Fig. 5b, where the scattering data in the equatorial x-axis (I_{EQ}) and meridian y-axis (I_{MER}) are plotted together with the azimuthally averaged scattering curve (I_{AA}). While both I_{EQ} and I_{MER} exhibit structural features at higher q-values, we see an additional correlation peak appearing along the y-axis for lower q-values. This low-q feature along the y-axis disappears at lower packing fractions, while the high-q structure peak persists to much lower ϕ values.

We now try to quantify these anisotropic features and normalize the scattering data along the equatorial and meridian axes with the azimuthally averaged scattering data. This results in the normalized data shown in Fig. 5c, where we now clearly recognise the anisotropic features of the scattering data. We finally calculate two effective order parameters λ_{EQ} and λ_{MER} as the product of the relative increase of scattered intensity (in either equatorial (x) or meridian (y) directions) and the peak amplitude of the measured structure factor $S_M(q^*)$ in the absence of a field for a given volume fraction ϕ:

$$\lambda_{EQ}(B,\phi) = S_M(q^*, B=0, \phi) \times \frac{I_{EQ}(q_{EQ}{}^*, B, \phi)}{I_{AA}(q_{EQ}{}^*, B, \phi)}; \quad (3)$$

$$\lambda_{MER}(B,\phi) = S_M(q^*, B=0, \phi) \times \frac{I_{MER}(q_{MER}{}^*, B, \phi)}{I_{AA}(q_{MER}{}^*, B, \phi)}. \quad (4)$$

Here it is important to note that the values of λ_{EQ} and λ_{MER} parameterize the contributions from both structural correlations (the term $S_M(q^*)$) and the asymmetry in such correlations (the term I_{EQ}/I_{AA} and I_{MER}/I_{AA} at the corresponding peak positions, respectively). The lower boundary of both order parameters is λ_{EQ} = 1 and λ_{MER} = 1 for a random isotropic orientation of the ellipsoids. The anisotropic scattering patterns measured throughout an entire magnetic field hysteresis loop allow for an easy characterisation of transitory states, the quenched order at the given field strength, and the annealed order upon returning to zero-field. By calculating the parameters λ_{EQ} and λ_{MER} we can thus directly monitor the evolution of positional and orientational correlations as a function of ϕ and B.

This is demonstrated in Fig. 6, which shows complete hysteresis loops of λ_{EQ} for several volume fractions, where the field strength has been varied from B = 0 T to B = 1 T, reversed to B = −1 T, and reversed again to B = 1 T, while performing *in situ* SAXS measurements in real time. For moderate packing fractions λ_{EQ} is completely reversible. The slope of $\lambda_{EQ}(B)$ at small fields and the height of the saturation plateau at high fields gradually increase with packing fraction. Particles are in a dynamic field-dependent equilibrium state, and their positional and orientational order only depends on the magnitude of the applied field, and no memory effects are visible. However, for ϕ = 0.59 this behaviour changes dramatically, and we now observe an open hysteresis loop. The orientational and

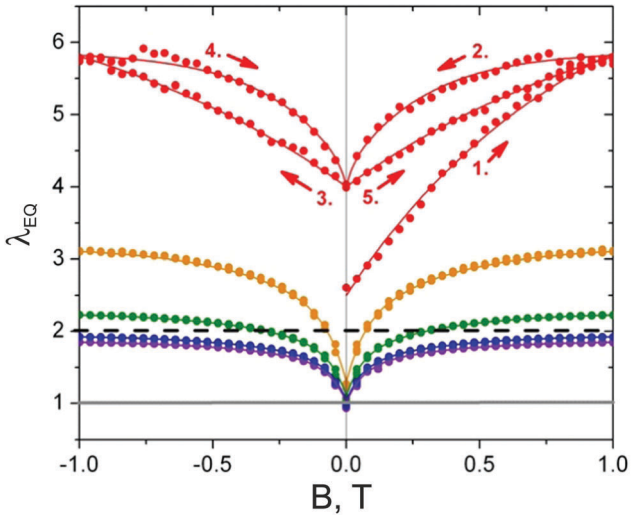

Fig. 6 Full hysteresis loops of the effective order parameter λ_{EQ}. Shown is a sequence using a range of magnetic field strength $-1 \leq B \leq +1$ T for a five-branch loop of λ_{EQ} for different volume fractions (ϕ = 0.59 plotted red, ϕ = 0.25 orange, ϕ = 0.19 olive, ϕ = 0.09 blue, ϕ = 0.04 violet). The grey line shows the limit of a fully disordered sample λ_{EQ} = 1. The dashed line indicates λ_{EQ} = 2 chosen as the threshold value for the formation of a polarised fluid. Arrows indicate the directions of the hysteresis branches. The curves are visual guides only.

positional order is now path-dependent, indicating a phase transition that results in a constrained rotational freedom of the ellipsoids. For ϕ = 0.77 (not shown) we find very high values of the effective order parameter (up to λ_{EQ} = 13) and a complex, path-dependent behaviour, that is clearly linked to the completely arrested state at zero field already apparent from the macroscopic flow behaviour (Fig. 4).

While these effective order parameters provide us with a simple means to compare structural correlations and the degree of anisotropy of different samples, similar to the Hansen–Verlet criterion[32] for crystallisation in hard sphere particle systems, and detect a phase transition from the formation of an opening of a hysteresis loop, we need additional information to clearly assign specific structures or phases to the given values of λ_{EQ} and λ_{MER}. We have thus performed Metropolis Monte Carlo (MC) simulations for a fluid of hard prolate spheroids with a constant axial ratio p = 2.3. We have looked at the effect of a homogeneous external magnetic field of strength B, represented by the interaction energy

$$U^{\mathrm{Ext}} = -B\sum_i \mu_i \cos\beta_i, \tag{5}$$

where β_i is the angle between the particle short (equatorial) axes of a particle i, which we refer to as the dipole axis, and the x-axis of the lab-frame coordinate system. The magnetic moments of the particles μ_i are taken to be equal to the experimental value for our hematite particles, and simulations were performed for B = 0, 0.04, and 0.24 T, respectively. These field values correspond to energy differences of $10 \leq U \leq 60k_BT$ between a parallel and a perpendicular orientation of the dipoles relative to the field.

We perform simulations at volume fractions ϕ = 0.53 and ϕ = 0.59, where the SAXS experiments indicate a phase transition, visible in the open hysteresis loop of the order parameter λ_{EQ} shown in Fig. 6. To further quantify the degree of orientational order we consider two order parameters. We first introduce a particle-centered nematic order parameter S_2^{N}

$$S_2^{\mathrm{N}} = \frac{1}{N(N-1)}\left\langle \sum_{i,j;i\neq j} P_2(\cos\theta_{ij}) \right\rangle, \tag{6}$$

where θ_{ij} is the angle between the long axes of particles i and j and P_2 is the second order Legendre polynomial. A random distribution of orientations gives S_2 = 0 and perfect nematic ordering gives S_2 = 1. This order parameter is sensitive to the alignment of the particles by the external field and is therefore not suitable to identify a traditional nematic phase for $B \neq 0$. Therefore, we also compute the 2D analogue of this parameter $S_2^{\mathrm{N}'}$,

$$S_2^{\mathrm{N}'} = \frac{1}{N(N-1)}\left\langle \sum_{i,j;i\neq j} C_2(\cos\theta_{ij}') \right\rangle, \tag{7}$$

where θ_{ij}' is the angle between the projections of particle long axes in the lab-frame yz-plane and C_2 is the second order Chebychev polynomial of the first kind. This order parameter is the 2D analogue of the 3D nematic order parameter S_2^{N}, and will indicate whether there is any orientational order perpendicular to the field axis.

The scattering pattern from the periodic simulated system is calculated using

$$I(\boldsymbol{q}) = \left\langle \left| \sum_j P\left(\boldsymbol{q}, \hat{\boldsymbol{L}}_j\right) e^{i\boldsymbol{q}\cdot\boldsymbol{r}_j} \right|^2 \right\rangle, \tag{8}$$

where $\boldsymbol{r}_i$ and $\hat{\boldsymbol{L}}_i$ are vectors describing the position and orientation, respectively, of particle j. The form factor P is taken from ref. 33. The scattering vectors $\boldsymbol{q}$ considered are $\left\{n_x\frac{2\pi}{L_B}, 0, n_z\frac{2\pi}{L_B}\right\}$ and $\left\{n_x\frac{2\pi}{L_B}, n_y\frac{2\pi}{L_B}, 0\right\}$ with all relevant combinations of n_x, n_y, n_z = 0, 1, 2,..., 25 excluding $\boldsymbol{q}$ = {0,0,0}. The equivalent y- and z-directions are averaged, resulting in an intensity distribution that depends on $q_{EQ} = q_x$ and $q_{MER} = \sqrt{q_y^2 + q_z^2}$.

The corresponding simulated scattering patterns and representative configurations are shown in Fig. 7. In the absence of an external magnetic field, we observe an isotropic fluid for both simulated volume fractions (ϕ = 0.53 and ϕ = 0.59). Therefore, the scattering pattern is axially symmetric. In both cases, the S_2^{N} and $S_2^{\mathrm{N}'}$ order parameters are zero to simulation accuracy.

For volume fraction ϕ = 0.53 in the presence of a magnetic field, the scattering pattern is now anisotropic, but the only source of anisotropy is the applied field. We still find $S_2^{\mathrm{N}'} = 0.0$, meaning that the fluid has no orientational order perpendicular to the field direction. The field-induced particle alignment gives rise to an increase in the height of the peak in scattering intensity in the x-direction. This can be ascribed to an enhanced positional order. When the particles are aligned with their long axis in the yz-plane there is no longer any

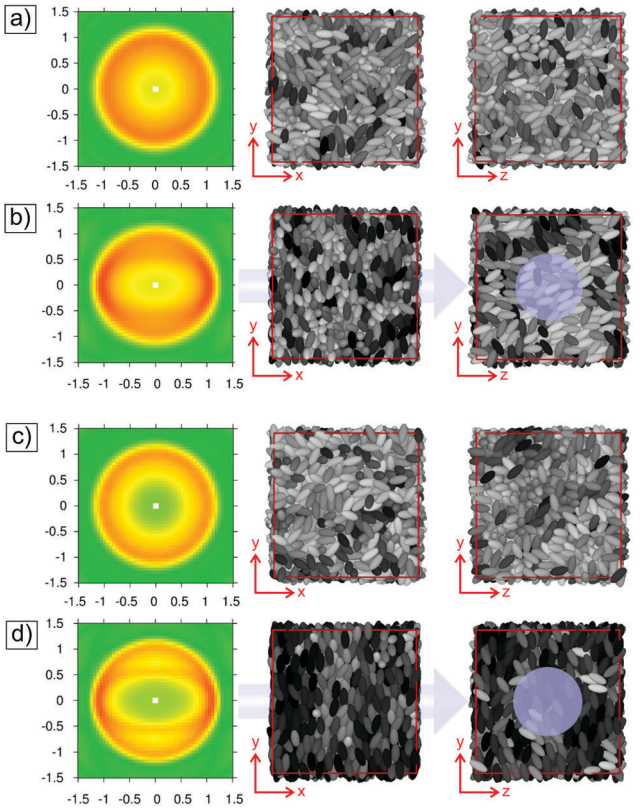

Fig. 7 Simulated scattering patterns and simulation snapshots. (a) ϕ = 0.53 at zero-field. (b) ϕ = 0.53 at B = 0.04 T. (c) ϕ = 0.59 at zero-field. (d) ϕ = 0.59 at B = 0.04 T. The middle column shows snapshots in the plane parallel to the field direction (x–y plane), whereas the right column shows the corresponding snapshots in a plane perpendicular to the field direction (y–z plane), and for systems with an applied field the field direction is also indicated by the light blue arrow. In the snapshots the particles are grey scale coded according to their orientation projected in the plane perpendicular to the field. Black indicates full alignment with respect to the average orientation in the snapshot.

orientational entropy cost associated with bringing two particles together along the x-direction. This permits an efficient sphere-like packing that gives the fluid a locally layered structure in the x-direction, that is reminiscent of the coordination shells seen for hard sphere fluids at high densities.

For volume fraction ϕ = 0.59 and B = 0.04 T the system develops into a field-induced nematic phase, for which there is orientational order perpendicular to the field direction expressed by a non-zero value of the order parameter of $S_2^{N'} = 0.36$. This is reflected in the scattering patterns by the appearance of a split peak in the yz-direction for the nematic state. The position of the innermost peak corresponds to particles aligned tip-to-tip, while the outermost peak corresponds to particles aligned side-to-side. Note that for this aspect ratio the nematic phase is not expected to be stable in the absence of a field at any volume fraction.[8] It is, however, intuitively reasonable that the alignment due to the field would favour the nematic phase. The isotropic to nematic phase transition occurs when the gain in positional entropy from aligning the particles outweighs the associated cost in orientational entropy. The orientational entropy is decreased by polarisation of an isotropic fluid and transition to a field-induced nematic phase is, therefore, favoured.

Bearing in mind these findings of the simulations and our experimental observations, we propose a criterion relating the experimental values of λ_{EQ} and λ_{MER} to specific phases of the ellipsoids. Similarly to the reasoning behind the static Hansen–Verlet criterion,[32] our definition is that such phases are present when λ_{EQ} or λ_{MER} exceed a threshold value.

Our data on the values characteristic for the transitions in the range $0.53 < \phi < 0.59$ lead us to suggest that the isotropic–nematic transition occurs when $\lambda_{MER} > 2$. We choose the exact threshold value of 2 because samples with a hysteresis behaviour have $\lambda_{EQ}(B = 0)$ and $\lambda_{MER}(B = 0)$ above 2, while the samples with no memory effects have both parameters at zero-field positioned below 2. An equally important reason for this assignment is the finding of the simulations that ϕ = 0.59 shows $S_2^{N'} = 0.36$ (field-induced nematic order) at very low fields, while ϕ = 0.53 always shows $S_2^{N'} = 0$ at any field strength. The third equally important reason is that $\lambda_{MER} > 2$ approximately coincides with the formation of a second-order peak in the y-axis on the detector, observed in both experiments and simulation and concomitant with the onset of the nematic phase in our simulations.

Fig. 8 depicts the resulting experimental phase diagrams of the ellipsoids in equatorial x-axis (a) and meridian y-axis (b) where the colour code represents the values of λ_{EQ} and λ_{MER}, respectively. In Fig. 8 we distinguish between an isotropic fluid (I), a polarised fluid (PF) ($\lambda_{EQ} > 2$) and a nematic (N) ($\lambda_{MER} > 2$) phase. Samples where the magnetic moments are aligned, *i.e.* where the particle director is perpendicular to an external field, in principle possess a field-induced nematic order. This can be seen in analogy to discotic liquid crystals, where the ellipsoids that rotate freely around their short axis represent on average discoids. However, we have chosen the term polarised fluid for this condition in order to distinguish them from systems where we observe a field-induced transition to a traditional nematic where there is orientational order for the particle director or long axis. For consistency, we plot these values for the case of an annealed order, *i.e.* when the samples were first brought to the maximum field. The values of ϕ and B where we experimentally observed the criterion λ_{EQ} = 2 are shown as open circles in Fig. 8a, and the values where we observed the criterion λ_{MER} = 2 are shown as open squares in Fig. 8b.

While the translational order between the short axes of the ellipsoids (λ_{EQ}) cannot be directly matched to any phase transition, it characterizes the degree of polarization of the particle suspension by the magnetic field in the region below the nematic transition. Magnetic field has a strong influence on λ_{EQ} in the ϕ–B coordinates. In particular, the contour (iso-) line λ_{EQ} = 2 is shifted to smaller packing fractions with increasing field. In the ϕ–B coordinates, this contour line has an asymptote at the packing fraction ϕ = 0.10, showing that the positional order of non-interacting short axes reaches a saturation and cannot be promoted further whatever field strength is applied. This experimental result reflects the strong coupling between

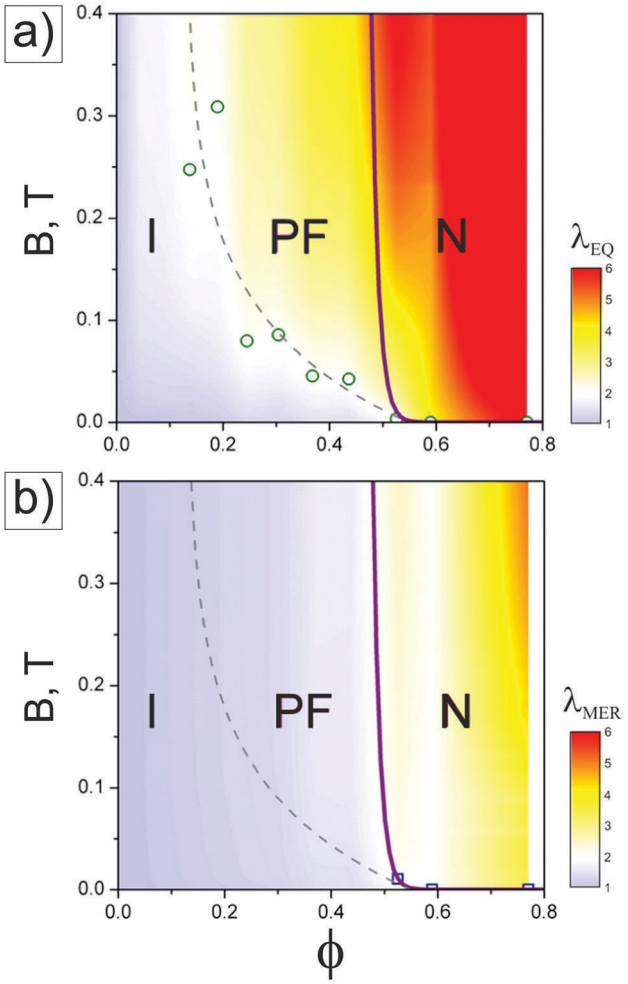

Fig. 8 Phase diagram of the ellipsoids, where we distinguish between an isotropic fluid (I), a polarised fluid (PF) and a nematic (N) phase. (a) Effective equatorial order parameter λ_{EQ} maps a family of contour lines where the field-induced alignment of the dipole axes results in a particular positional correlation along the x-axis. The values of ϕ and B where we experimentally observed the criterion $\lambda_{EQ} = 2$ are shown as open circles. The dashed line in both figures is a representative contour line $\lambda_{EQ} = 2$. The corresponding colour code for λ_{EQ} is given on the right hand side of the graph. (b) The effective meridian order parameter λ_{MER} allows mapping the nematic transition ($\lambda_{MER} = 2$) as shown by the solid line in both figures. The values of ϕ and B where we experimentally observed the criterion $\lambda_{MER} = 2$ are shown as open squares. The corresponding colour code for λ_{MER} is given on the right hand side of the graph.

particle–particle and particle–field interactions, in a context where the field only enforces alignment of short axes of the ellipsoids. This is an unusual example of field-assisted assembly where the field reduces the rotational freedom and excluded volume of each particle in a complex manner and thus contributes to the equatorial positional correlations without directly enforcing the order of the long axes.

These particular features of a polarised fluid can be nicely illustrated with a simulation at $\phi = 0.1$, *i.e.* close to the boundary of the formation of a polarised fluid. Snapshots of suspensions at zero field and $B = 0.24$ T are shown in Fig. 9. For $B = 0$ particles are randomly oriented and show relatively weak

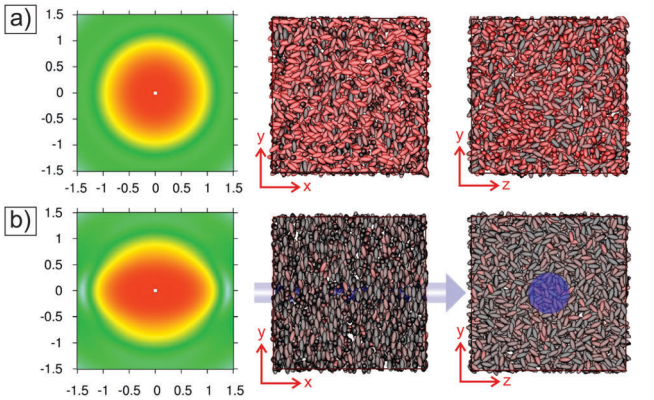

Fig. 9 Simulated scattering patterns and simulation snapshots of the ellipsoids at a packing fraction of $\phi = 0.1$, where particles are colour coded according to their orientation given by $\hat{\boldsymbol{L}}$ with respect to the field or x-axis: grey for $\hat{\boldsymbol{L}} \perp \boldsymbol{B}$ and red for $\hat{\boldsymbol{L}} \parallel \boldsymbol{B}$. (a) Zero-field case, particles are randomly oriented and show relatively weak positional correlations only. (b) Field $B = 0.24$ T, where the particles are fully aligned with their magnetic moment along the field axis given by the light blue arrow. The middle column shows snapshots in the plane parallel to the field direction (x–y plane), whereas the right column shows the corresponding snapshots in a plane perpendicular to the field direction (y–z plane).

positional correlations only. At $B = 0.24$, however, the particles are now fully aligned with their magnetic moment parallel to the field axis, and their long axis rotating freely around the field axis, *i.e.* in the yz-plane. This results in a layered suspension structure, creating an anisotropic correlation peak along the field axis, but only weak positional order within the yz-plane.

The translational order between the long axes of the ellipsoids (λ_{MER}) characterizes the isotropic–nematic transition. In the ϕ–B coordinates, the I–N borderline is nearly field-independent: it starts from a vertical asymptote estimated at no less than $\phi = 0.50$ at a high B, rapidly descends to $B = 0.01$ T at $\phi = 0.53$, and then reaches a zero-field level at a point below $\phi = 0.59$. This is in a reasonable agreement with our simulations that demonstrated, for this narrow range of packing fractions, snapshots of a field-induced nematic order that is cancelled when the field is removed. However, experimentally we find evidence that the sample with $\phi = 0.59$ is already nematic at $B = 0$, in contrast to the simulations. There are several reasons for this discrepancy between experiments and simulations. Determining volume fractions experimentally is prone to uncertainties in particular at very high densities. The exact value of the axial ratio ρ relies on a knowledge of the thickness of the outermost PAA shell, which again is prone to uncertainty. Moreover, as the thickness of a polyelectrolyte layer is dependent on the ionic strength, which also changes with concentration, the effective value of ρ may slightly change with ϕ. Finally, although electrostatic interactions are strongly screened by the counterions, there is nevertheless some weak additional electrostatic contribution from the PAA, which could also shift the I–N transition slightly to lower ϕ. While these uncertainties connected to the effective particle dimensions and interactions are small, they could still make a significant difference in this particular region of the phase diagram very close to the lower

limit of the existence of a stable nematic phase and a possible I–N–SM2 coexistence.

There remains in fact the question whether our system at ϕ = 0.77 may already be in a SM2 crystal phase. The earlier numerical simulations of the phase diagram including analysis or stability of various solid structures,[12] and the arrested nature of the sample at ϕ = 0.77 would indeed not rule out the possibility that this dense phase is an SM2 crystal. Moreover, our simulations do not exclude the stability of an SM2 crystal even at ϕ = 0.59. Additionally, a dramatic smearing of a crystalline diffraction pattern due to polycrystallinity and particle polydispersity would render it difficult to distinguish the SAXS pattern of a nematic orientational glass from that of a polycrystalline SM2, when looking only at the qualitative features. However, our simulations demonstrated that a hypothetical N–SM2 transition would be characterised by a considerable shift in the first-order peak position q^* towards higher q-values should crystallisation happen. There is nothing suggestive of such a transition in our experiments where q^* is independent of B at ϕ = 0.59 and ϕ = 0.77. This indicates that no SM2 forms, possibly because of polydispersity, but also because the system does not easily crystallise from a jammed nematic state.

3.3 Magnetic bulk properties

We finally investigate whether the structural transitions observed with SAXS also manifest themselves in the macroscopic magnetic response of the suspensions. The magnetic behaviour of the suspensions measured in the axis of the applied magnetic field (x-axis) is summarised in Fig. 10. It is important to stress that we expect bulk magnetic properties of the suspensions that primarily reflect the interplay between Brownian motion and a field-induced alignment of the magnetic moments of the particles, and not so much the magnetic behaviour of the individual particles, which has been characterised in detail previously.[18]

Fig. 10A shows the magnetisation of all samples normalised by their total mass content of hematite. The mass content is calculated through the mass concentration of each sample, and the average mass fraction α of hematite inside one particle. Fig. 10A clearly demonstrates that the magnetisation curves for the low and moderate ϕ nearly overlap, while the samples with packing fractions ϕ = 0.59 and ϕ = 0.77 show progressively decreasing magnetisation. These results may be interpreted as a transition from free alignment of magnetic moments to a dynamic arrest, concomitant with the onset of magnetic ordering, where the magnetic field is insufficient to fully align each magnetic moment. Here it is important to emphasise that the polarised state with aligned dipole axes of the ellipsoids at ϕ = 0.53 is triggered by the magnetic field only. Brownian relaxation cancels the order when the field is removed, and there is no structural hysteresis observed in the magnetic field loop SAXS measurements. However, topological constraints and a likely rotational arrest that occurs for $\phi > 0.53$ drastically changes this behaviour. The relaxation times for the particles grow by many orders of magnitude and the structural features persist after the magnetic field is turned off.

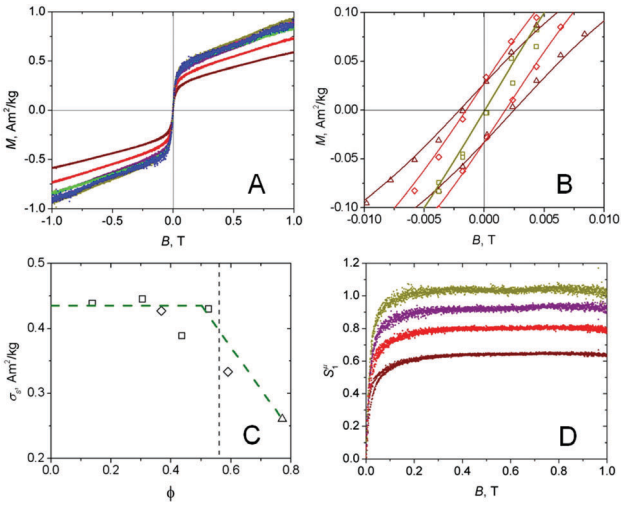

Fig. 10 Bulk magnetic properties of the particle suspensions. (A) Net magnetisation is nearly independent on packing fraction for $\phi \leq 0.53$ (ϕ = 0.14: blue; ϕ = 0.30: dark yellow; ϕ = 0.37: green; ϕ = 0.44: purple; ϕ = 0.53: pink), but shows a progressive decay for ϕ = 0.59 (plotted red) and p = 0.77 (plotted wine). (B) Same data magnified to highlight regime around B = 0, the data reveal ferromagnetic-type hysteresis loops for $\phi \geq 0.59$ yet no hysteresis for ϕ = 0.30. (C) Saturation magnetisation decreases with packing fraction. (D) The Langevin-type behaviour of the first-rank orientational order parameter S_1^u reveals the saturation plateau decreasing with packing fraction. Plotted are ϕ = 0.77 (wine), ϕ = 0.59 (red), ϕ = 0.44 (purple), ϕ = 0.30 (dark yellow).

The magnetisation behaviour at low fields as seen in Fig. 10B shows that samples with $\phi \geq 0.53$ demonstrate hysteresis with a non-vanishing remanent magnetisation and a non-zero surface area of the hysteresis loop. Also shown in the same figure is the magnetisation for ϕ = 0.30, which has a closed loop. The sample with ϕ = 0.53, not plotted in Fig. 10B, showed slight indications of a loop opening.

To describe the measured magnetisation, we take into account the non-zero high-field susceptibility that we earlier related to the contribution of the weak antiferromagnetic susceptibility of single domain hematite,[17] which is added as a linear term to the Langevin equation:[34]

$$M(B) = \sigma_s \cdot \left(\coth \frac{\mu B}{k_B T} - \frac{k_B T}{\mu B} \right) + \frac{B \chi_{HF}}{\mu_0}, \qquad (9)$$

where σ_s is the saturation magnetisation and χ_{HF} the high-field magnetic susceptibility.

Fig. 10C shows the dependence of the saturation magnetisation σ_s on ϕ as determined by the modified Langevin fit to the individual data sets for each ϕ. The decrease in the saturation magnetisation can be explained in terms of the freedom of the particles to align fully with the directing field. Below ϕ = 0.53, the magnetic field aligns the magnetic moments of the individual particles along the field lines resulting in a maximum macroscopic magnetisation that is proportional to particle concentration. The decrease of σ_s is a result of the reduced ability of the particles to align with the external field. Additionally, σ_s allows to determine the individual magnetic moment of one particle from the dilute-regime plateau σ_s = 0.4455 A m^2 kg^{-1}

and the mass of hematite within the average particle (m_h = 2.325 × 10^{-18} kg) *via* $\mu = \sigma_s \cdot m_h$. The resulting magnetic moment μ = 1.036 × 10^{-18} A m^2 is in reasonable agreement with the values previously found for similar particles.[17]

This behaviour of the magnetic properties is in an excellent agreement with the SAXS data where we find structural hysteresis and persisting order for $\phi > 0.53$. Below the arrest transition, the magnetising field directs each particle magnetic moment along the field lines, resulting in a non-zero measured magnetisation. Small fields, however, are insufficient to overcome Brownian motion that randomises the direction of magnetic moments, and at $B = 0$ the system becomes fully isotropic with the individual magnetic moments cancelling each other. This combination of zero remanence, closed hysteresis loops and higher saturation magnetisation are features of superparamagnetic behaviour for the suspension. At high volume fractions, however, the particles possess orientational order and a characteristic center-to-center separation that only slightly exceeds the minimally possible distance between compressed ellipsoids along their equatorial axes. Rotational freedom is then restricted and the system of particles exhibits a magnetic memory and the ferromagnetic features (open magnetisation curve and a non-zero, yet weak, remanent magnetisation) typical for bulk hematite.

In a next step we use the magnetisation data to determine the order parameter of the magnetic moments. Orientational order parameters are commonly defined in terms of an average over the nth-order Legendre polynomial for a particular orientational distribution. We will follow a definition[17,35] for the order parameter S_1^μ as a temporal and orientational average over the first-order Legendre polynomial $P_1^0(\cos\beta) = \cos\beta$, where β is angle between a magnetic moment and the aligning field and $f(\beta)$ is the orientational distribution function:

$$S_1^\mu = \langle \cos\beta \rangle = \frac{\int_0^\pi \cos\beta \cdot f(\beta) \sin\beta \mathrm{d}\beta}{\int_0^\pi f(\beta) \sin\beta \mathrm{d}\beta}. \quad (10)$$

Since S_1^μ corresponds to an average scalar product of these two vectors normalised by their magnitudes, $S_1^\mu = \left\langle \frac{\vec{\mu}}{\mu} \cdot \frac{\vec{B}}{B} \right\rangle$, it can be computed from the directly measured magnetisation data.[17] The values of the order parameter are bounded by $S_1^\mu = 0$ for a random isotropic orientation of the magnetic moments, and $S_1^\mu = 1$ for a fully aligned sample. Based on an earlier finding for similar particles that the high-field susceptibility of the particles is isotropic and makes no contribution to the order, as shown by torque measurements,[17] we can compute the order parameter *via*

$$S_1^\mu(B) = \frac{\mu_0 \cdot M(B) - B\chi_{HF}}{\mu_0 \cdot \sigma_s}. \quad (11)$$

Fig. 10D summarises the resulting order parameters for different volume fractions where we use σ_s from the dilute plateau but χ_{HF} determined individually for each ϕ. Fig. 10D shows that the magnetic moments reach a saturated level of alignment at moderate fields and generally follow a Langevin-like behaviour. The decreasing saturation levels of S_1^μ can be interpreted as a topological constraint to realign and direct particles in each dense nematic domain.

The observed superparamagnetic magnetisation is neither a latent property of a single particle, nor a property of crystalline hematite as such, but an ensemble behaviour of particles as a result of the interplay between the alignment of magnetic moments and Brownian motion. A restricted rotational degree of freedom and slow dynamics, observed at $\phi \geq 0.59$, results in the appearance of the typical signatures of a ferromagnetic response: an open magnetisation curve and a non-zero, yet weak, remanent magnetisation.

It is, however, important to not only measure magnetisation loops, but also investigate the time-resolved relaxation of the magnetisation for the dense samples ϕ = 0.59 and ϕ = 0.77. This will allow us to distinguish slow relaxation of the magnetic moment after a change in the external field from a true ferromagnetic bulk behaviour of these systems. The resulting relaxation curves are plotted in Fig. 11. After an exposure to a high field B = 1 T, the field is instantly turned off during a transition time of less than 50 ms. We then measure the remanent magnetisation during 500 s in steps of 0.1 s.

To understand the results of Fig. 11 it is important to recall that the irreversible relaxation of magnetisation after a sudden change of the external field for a broad range of magnetic materials often follows linear-logarithmic law characterised by a so called magnetic viscosity:[36]

$$M(t) = -S \log(t/t_0) + \text{const.}, \quad (12)$$

where S is the coefficient of magnetic viscosity. As seen in Fig. 11, the remanent magnetisation for ϕ = 0.77 does not decay exponentially or through a stretched exponential relaxation, which would be the case if relaxation were to occur *via* Brownian motion, but instead follows eqn (12) with S = 0.00536 A m^2 kg^{-1}

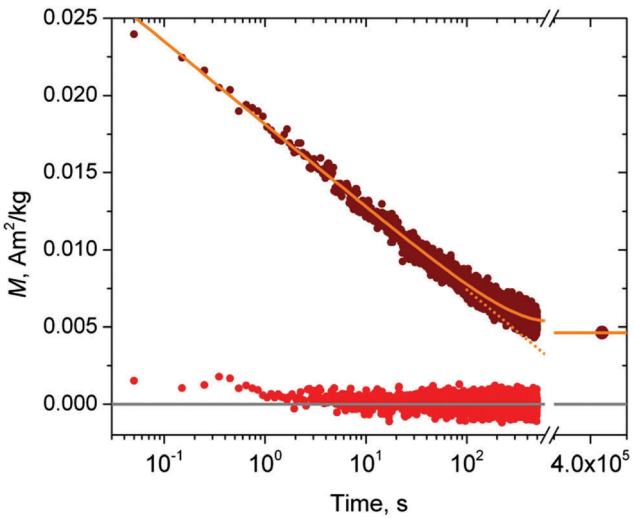

Fig. 11 Magnetic relaxation behaviour for ϕ = 0.59 (red) and ϕ = 0.77 (wine). The dotted and solid lines fits to a logarithmic time dependence without and with a constant term as given in eqn (12). Note the long-time limit value for ϕ = 0.77 recorded after 5 days of demagnetisation.

for most of the observed demagnetisation data. At long times it then deviates and levels off after *ca.* 100 s. We have independently measured the persisting remanent magnetisation with a 2G SQUID rock magnetometer after 5 days of demagnetisation as plotted in the right hand part of Fig. 11. We thus find the natural remanent magnetisation, M_{NR} = 0.00464 A m^2 kg^{-1}. The short-time limit of $M(t)$ gives a value of the remanent magnetisation of *ca.* 0.025 A m^2 kg^{-1}, slightly lower than what has been measured in a full hysteresis loop in Fig. 10B. This indicates that our loop measurements in Fig. 10B were not quasi-static, and that the sample was not allowed to completely relax when brought through the zero-field region during the rapid measurement of the loop.

The remanent magnetisation for ϕ = 0.59 measured in the field loop is σ_R = 0.025 A m^2 kg^{-1} (Fig. 10B). However, the demagnetisation experiments show that we obviously lose most of the remanent magnetisation after less than 0.1 s and do not observe a magnetoviscous relaxation. While the sample at ϕ = 0.59 is still fluid-like (Fig. 4), Brownian relaxation obviously is slowed down significantly such that the hysteresis loop opens. However, this remanent magnetisation (Fig. 11) relaxes immediately after the removal of the field and decays to values close to zero on a time scale of less than 0.1 s.

4 Conclusions

The peculiar magnetic properties of the ellipsoidal hematite particles result in quite unusual field effects, and have allowed us to identify distinctly different isotropic (I), polarised (PF) and inherently polarised nematic (N) phases as a function of packing fraction and magnetic field strength. The source of this assembly pattern lies in the fact that a magnetic field aligns the individual magnetic moments and thus the direction of the short particle axes of the particles only. Therefore, a positional order in a polarised phase is complex and not quite intuitive. While the field-to-particle interaction induces an orientational order of the short axes along the *y*-direction, the scattering patterns indicate an instant onset of positional order with a characteristic length given by the short axis. To understand this result, we had to consider both particle–field and particle–particle interactions. While the field constrains the short axes of the ellipsoids, the particle-to-particle interaction also constrains the long axes of the ellipsoids. The combined effects of both interactions then result in a situation where positional correlations are coupled to field-induced orientational correlations. At low and intermediate ϕ-values, this field-induced polarisation and the resulting positional correlations are destroyed by thermal relaxation as soon as the field is removed. However, complex dynamic memory effects, absent elsewhere, are found above the threshold to the nematic phase. Particularly interesting is the fact that this structural transition is also reflected in the bulk magnetic properties of the suspensions, which accordingly change from a superparamagnetic to a ferromagnetic behaviour. We can look at this as an analogy to the Curie point for ferromagnets, as in both cases thermal fluctuations can overrun the collective orientational order of individual magnetic moments and change the overall magnetic behaviour of the system, *i.e.* we extend the often used colloid-atom analogy also to magnetic properties or spin systems.

Acknowledgements

We thank Mikhail Karnevskiy for the numerical script to locate the positions of maxima on scattering curves, and Mathias Reufer for the numerical script to simulate the form factor of core–shell ellipsoids. We acknowledge Mathias Reufer, Priti S. Mohanty, and Sven Dorosz for helpful discussions, Liliane Ackermann Hirschi for the help with the synthesis of the particles, and Teemu Ikonen for technical assistance during the SAXS data acquisition. The SAXS experiments were conducted at the cSAXS beamline of the Swiss Light Source, Paul Scherrer Institute, Switzerland. Financial support from the Adolphe Merkle Foundation, the Swiss National Science Foundation, the SoftComp network, the Science Faculty of Lund University, the Swedish Research Council (Project 621-2011-4338 and the Linnaeus Center of Excellence on Organizing Molecular Matter), the European Research Council (ERC-339678-COMPASS), and the Knut and Alice Wallenberg Foundation (project grant KAW 2014.0052) is gratefully acknowledged.

References

1 S. C. Glotzer and M. J. Solomon, *Nat. Mater.*, 2007, **6**, 557–562.
2 L. Onsager, *Ann. N. Y. Acad. Sci.*, 1949, **51**, 627–659.
3 B. Tjipto-Margo and G. T. Evans, *J. Chem. Phys.*, 1990, **93**, 4254–4265.
4 D. Frenkel, B. M. Mulder and M. Tague, *Phys. Rev. Lett.*, 1984, **52**, 287–290.
5 D. Frenkel and B. M. Mulder, *Mol. Phys.*, 1985, **55**, 1171–1192.
6 P. Bolhuis and D. Frenkel, *J. Chem. Phys.*, 1997, **106**, 666–687.
7 M. Letz, R. Schilling and A. Latz, *Phys. Rev. E: Stat. Phys., Plasmas, Fluids, Relat. Interdiscip. Top.*, 2000, **62**, 5173.
8 G. Odriozola, *J. Chem. Phys.*, 2012, **136**, 134505.
9 G. Bautista-Carbajal, A. Moncho-Jordá and G. Odriozola, *J. Chem. Phys.*, 2013, **138**, 064501.
10 A. Bezrukov and D. Stoyan, *Part. Part. Syst. Charact.*, 2006, **23**, 388–398.
11 P. Pfleiderer, K. Milinkovic and T. Schilling, *Europhys. Lett.*, 2008, **84**, 16003.
12 M. Radu, P. Pfleiderer and T. Schilling, *J. Chem. Phys.*, 2009, **131**, 164513.
13 A. A. Shah, H. Kang, K. L. Kohlstedt, K. H. Ahn, S. C. Glotzer, C. W. Monroe and M. J. Solomon, *Small*, 2012, **8**, 1551–1562.
14 J. J. Crassous, H. Dietsch, P. Pfleiderer, V. Malik, A. Diaz, L. A. Hirshi, M. Drechsler and P. Schurtenberger, *Soft Matter*, 2012, **8**, 3538–3548.
15 J. J. Crassous, A. M. Mihut, E. Wernersson, P. Pfleiderer, J. Vermant, P. Linse and P. Schurtenberger, *Nat. Commun.*, 2014, **5**, 5516.
16 S. Sacanna, L. Rossi, A. Wouterse and A. P. Philipse, *J. Phys.: Condens. Matter*, 2007, **19**, 376108.

17 M. Reufer, H. Dietsch, U. Gasser, A. M. Hirt, A. Menzel and P. Schurtenberger, *J. Phys. Chem. B*, 2010, **114**, 4763–4769.
18 M. Reufer, H. Dietsch, B. Gasser, U. Grobety, A. M. Hirt, V. K. Malik and P. Schurtenberger, *J. Phys.: Condens. Matter*, 2011, **23**, 065102.
19 I. Martchenko, H. Dietsch, C. Moitzi and P. Schurtenberger, *J. Phys. Chem. B*, 2011, **115**, 14838–14845.
20 C. Rufier, M. Reufer, H. Dietsch and P. Schurtenberger, *Langmuir*, 2011, **27**, 6622–6627.
21 M. Grzelczak, J. Vermant, E. M. Furst and L. M. Liz-Marzan, *ACS Nano*, 2010, **4**, 3591–3605.
22 P. S. Mohanty, A. Yethiraj and P. Schurtenberger, *Soft Matter*, 2012, **8**, 10819–10822.
23 S. Nöjd, P. S. Mohanty, P. Bagheri, A. Yethiraj and P. Schurtenberger, *Soft Matter*, 2013, **9**, 9199–9207.
24 P. S. Mohanty, P. Bagheri, S. Nöjd, A. Yethiraj and P. Schurtenberger, *Phys. Rev. X*, 2015, **5**, 011030.
25 H. Dietsch, V. Malik, M. Reufer, C. Dagallier, A. Shalkevich, M. Saric, T. Gibaud, F. Cardinaux, F. Scheffold, A. Stradner and P. Schurtenberger, *Chimia*, 2008, **62**, 805–814.
26 P. Pfleiderer and T. Schilling, *Phys. Rev. E: Stat., Nonlinear, Soft Matter Phys.*, 2007, **75**, 020402.
27 M. Ocaña, M. P. Morales and C. J. Serna, *J. Colloid Interface Sci.*, 1999, **212**, 317–323.
28 C. Graf, D. L. J. Vossen, A. Imhof and A. van Blaaderen, *Langmuir*, 2003, **19**, 6693–6700.
29 J. W. Perram and M. S. Wertheim, *J. Comp. Physiol.*, 1985, **58**, 409–416.
30 A. Donev, F. H. Stillinger, P. M. Chaikin and S. Torquato, *Phys. Rev. Lett.*, 2004, **92**, 255506.
31 C. W. Pester, M. Ruppel, H. G. Schoberth, K. Schmidt, C. Liedel, P. van Rijn, K. A. Schindler, S. Hiltl, T. Czubak, J. Mays, V. S. Urban and A. Böker, *Adv. Mater.*, 2011, **23**, 4047–4052.
32 J.-P. Hansen and L. Verlet, *Phys. Rev.*, 1969, **184**, 151.
33 L. C. Roess and C. G. Shull, *J. Appl. Phys.*, 1947, **18**, 308.
34 P. Langevin, *J. Phys. Theor. Appl.*, 1905, **4**, 678–693.
35 P. Ilg, M. Kröger and S. Hess, *J. Chem. Phys.*, 2002, **116**, 9078–9088.
36 D. V. Berkov and R. Kötitz, *J. Phys.: Condens. Matter*, 1996, **8**, 1257–1266.